

Surface electronic states in three-dimensional SnO₂ nanostructures

S. O. Kucheyev,* T. F. Baumann, P. A. Sterne, Y. M. Wang, T. van Buuren, A. V. Hamza, L. J. Terminello, and T. M. Willey
Lawrence Livermore National Laboratory, Livermore, California 94550, USA

(Received 2 March 2005; published 1 July 2005)

The electronic structure of three-dimensional SnO₂ nanostructures (aerogels) is studied by soft x-ray absorption near-edge structure (XANES) spectroscopy. High-resolution O *K*-edge and Sn *M*₃₋ and *M*_{4,5}-edge XANES spectra of monolithic nanocrystalline rutile SnO₂ aerogels with different surface areas (i.e., different surface-to-volume atom fractions) are compared with spectra of full-density rutile SnO₂ and tetragonal SnO. Spectra are interpreted based on the electronic densities of states in SnO₂ calculated with both cluster (self-consistent real-space multiple scattering) and band-structure (linear muffin-tin orbital) methods. Results show that, in contrast to the currently widely accepted picture, the presence of undercoordinated surface atoms not only affects the Fermi level position but also changes the structure of the conduction band by introducing additional Sn-related electronic states close to the conduction band minimum. These additional states are due to oxygen deficiency and are attributed to a surface reconstruction of SnO₂ nanoparticles forming the aerogel skeleton. Results of this study are important for understanding the physical processes underlying the performance of gas sensors based on SnO₂ nanostructures.

DOI: [10.1103/PhysRevB.72.035404](https://doi.org/10.1103/PhysRevB.72.035404)

PACS number(s): 71.20.Nr, 71.55.Ht, 78.70.Dm, 82.80.Pv

Tin dioxide (SnO₂) is a wide band gap semiconductor with a room-temperature band gap of ~ 3.6 eV. It is a prototype transparent conductor¹ and a model system for metal-oxide-based gas sensors.² Doped SnO₂ is also used in lithium batteries.³ Additional large interest in this material has recently been stimulated by the demonstration of room-temperature ferromagnetism in SnO₂ doped with 3*d* transition metal impurities^{4–6} and by the fabrication of various quasi-one-dimensional nanostructures, such as nanobelts and nanoribbons.^{7–9}

Most applications of SnO₂ are based on its specific surface and/or bulk electronic properties. Numerous previous studies have, therefore, focused on understanding the fundamental electronic structure of bulk and selected low-index surfaces of SnO₂ (see, e.g., Refs. 10–23). However, in almost all previous experimental reports,^{13–16} only occupied electronic states (i.e., the valence band region and core levels) have been studied. Hence, a comparison of the experiment and theory has been done for the valence band states only.^{17–19} There are only few previous experimental studies of unoccupied states in bulk SnO₂ reporting O *K*-edge x-ray absorption near-edge structure (XANES) spectra (which reflect the O *p*-projected contribution to the conduction band) with qualitative peak assignments.^{21–23} Very recently, Moreno *et al.*²³ reported a study of unoccupied electronic states in bulk SnO and SnO₂ by electron energy loss spectroscopy focusing on understanding O *K* edge. However, they²³ were not able to adequately describe the fine structure of the O *K* edge of SnO₂ with the real-space multiple scattering (RSMS) method.²⁴

Tremendous current interest in SnO₂ nanostructures has been stimulated by a possibility to develop a new generation of high-performance devices including gas and bio sensors, batteries, and catalysts. However, the fundamental electronic structure of low-dimensional SnO₂ remains essentially unexplored. Most of recent numerous reports have focused on the synthesis, structural properties, (UV-visible) optical absorp-

tion, and valence band states of SnO₂-based nanomaterials.^{2,7–9,25} The structure of the conduction band of SnO₂-based nanomaterials, which plays an important role in conductivity and gas sensing mechanisms, has not been investigated.

In this paper, we study the structure of the conduction band in SnO₂ aerogels by XANES spectroscopy. Such aerogels are open-cell solid foams derived from highly cross-linked wet gels by drying them under supercritical conditions.²⁶ These monolithic foams are characterized by a high degree of porosity ($\geq 90\%$), with ultrafine (nanometer scale) cells/pores. Our results show that, in contrast to the currently widely accepted picture,^{1,2} the presence of undercoordinated surface atoms not only affects the Fermi level position but also changes the structure of the conduction band by introducing additional Sn-related electronic states close to the conduction band minimum. These findings are important for understanding the physical processes underlying the performance of gas sensors based on SnO₂ nanostructures.

The SnO₂ aerogels were prepared based on an epoxide-initiated gelation method, as described in Ref. 27. The average density of as-synthesized aerogels was $\sim 3\%$ of the full density rutile SnO₂. Reference rutile SnO₂ and tetragonal SnO powders (with grain sizes ≥ 5 μm) were obtained from Sigma-Aldrich Corp. As-synthesized aerogels were annealed for 1 h in air at temperatures from 250 up to 550 °C. The microstructure of aerogels was studied by x-ray diffraction (XRD, with a CuK α source) and transmission electron microscopy (TEM). The TEM analysis was performed in a Philips CM300FEG microscope operating at 300 kV. Surface area determination and pore volume analysis were performed by Brunauer-Emmett-Teller (BET) and Barrett-Joyner-Halenda (BJH) methods using an ASAP 2000 Surface Area Analyzer (Micromeritics Instrument Corp.), as described in Ref. 28.

The XANES experiments were performed at both undulator beamline 8.0 at the Advanced Light Source and

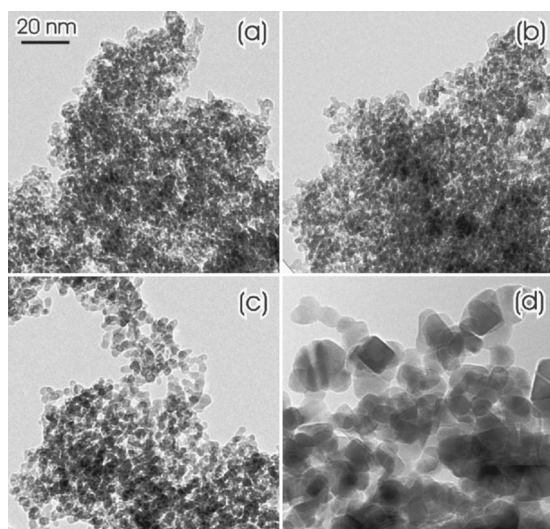


FIG. 1. Bright-field TEM images of SnO_2 aerogels annealed at temperatures of (a) 20, (b) 250, (c) 400, and (d) 550 °C. All four images are of the same magnification.

bending-magnet beamline 8-2 at Stanford Synchrotron Radiation Laboratory. Spectra were obtained by measuring the total electron yield (TEY), by monitoring the total sample photocurrent. The incoming radiation flux was monitored by the total photocurrent produced in a highly transmissive Au mesh inserted into the beam. The overall experimental resolution around O K , Sn $M_{3,5}$, and Sn $M_{4,5}$ edges was ~ 0.4 , ~ 1.0 , and ~ 0.4 eV, respectively. After a constant background subtraction, all spectra were normalized to the post-edge step heights.

Partial density of states (PDOS) in bulk rutile SnO_2 was calculated with both a cluster self-consistent RSMS method (with the FEFF code, version 8.20)²⁴ and a band-structure linear muffin-tin orbital (LMTO) method.²⁹ In FEFF calculations, clusters of 229 atoms and overlapping muffin tins were used. Both Sn and O potentials were calculated self-consistently within a 5-Å radius, and core holes were fully shielded (i.e., not included in calculations).³⁰ The LMTO calculations were performed in the atomic sphere approximation with six empty spheres in the unit cell. The angular momentum expansions included up to f , d , and p states for the Sn, O, and empty spheres, respectively. Tin $5s$, $5p$, and $5d$ states were all treated as valence states, as were the O $2s$ and $2p$ states. The valence states were treated semirelativistically, and the core states were recalculated self-consistently using a fully relativistic bound-state solver. The PDOS are not significantly altered when spin-orbit coupling is included in the valence band calculation. The calculations used 168 k points in the irreducible wedge for self-consistency, and a larger grid of 1326 irreducible k points to compute the densities of states in the tetrahedron method. The calculated RSMS and LMTO PDOS were both broadened for a better comparison with experimental data.

The morphology evolution of aerogels during thermal annealing is illustrated in TEM images in Fig. 1. Figure 1(a) shows that the skeleton of the as-prepared aerogel is formed by interconnected particles, ~ 3 – 5 nm in size. In addition, XRD, TEM selected-area diffraction (SAD), and high-

TABLE I. BET surface area (SA), pore volume (PV), and average pore diameter (APD) obtained from nitrogen desorption measurements for SnO_2 aerogels annealed at different temperatures (T^{ann}).

T^{ann} (°C)	SA ($\text{m}^2 \text{g}^{-1}$)	PV ($\text{cm}^3 \text{g}^{-1}$)	APD (nm)
20	320	1.85	21.5
250	474	2.97	21.9
400	157	1.44	30.7
550	55	1.15	48.4

resolution TEM analyses of both as-prepared and annealed aerogels indicate that the SnO_2 nanoparticles forming the aerogel solid network have the rutile (cassiterite) structure and are randomly oriented. No evidence of the tetragonal (romarchite) SnO phase has been revealed in our aerogels by XRD and SAD analyses.

Figure 1 also shows that annealing at temperatures ≤ 400 °C has a negligible effect on the average size of nanocrystals. For these annealing conditions, aerogels remain monolithic. However, Fig. 1(d) clearly shows that, during annealing at 550 °C, nanoparticles experience agglomeration and faceting. Such an increase in the nanoparticle size up to ~ 15 nm [Fig. 1(d)] is also accompanied by a collapse of monolithic samples into powders. This behavior is consistent with previous reports on thermal processing of sol-gel-derived SnO_2 nanomaterials.²

Table I summarizes results of the BET/BJH nitrogen adsorption/desorption analysis for annealed aerogels. It is seen from Table I that thermal annealing at temperatures above ~ 250 °C results in an expected decrease in surface area and an associated decrease in the average pore volume and an increase in the pore diameter. However, aerogels annealed even at 550 °C still exhibit a relatively high surface area of $55 \text{ m}^2 \text{g}^{-1}$.³¹ These BET/BJH results are consistent with TEM data from Fig. 1. A decrease in the surface area (and, hence, the fraction of undercoordinated surface atoms) with increasing annealing temperature is accompanied by a shrinkage of aerogel monoliths, and, for a temperature of 550 °C, by a collapse of the aerogel superstructure (from a monolithic solid into a powder).

Figure 2 shows XANES spectra over O K and Sn $M_{4,5}$ absorption edges of annealed aerogels. Within the dipole approximation,³² such O K - and Sn $M_{4,5}$ -edge spectra reflect electron transitions from the O $1s$ and Sn $3d$ (spin-orbit split into $3d_{3/2}$ and $3d_{5/2}$ levels, giving rise to M_4 and M_5 edges, respectively) core levels, respectively, into unoccupied electronic states above the Fermi level. If possible core-hole relaxation and electron correlation effects and higher multipole transitions are ignored, such spectra essentially map O-related p -projected (O K edge) and Sn-related p - and f -projected (Sn $M_{4,5}$ edge) states in the conduction band.³³ Figure 2 shows that O K -edge features are broadened for the as-prepared aerogel and become progressively sharper with increasing annealing temperature (and, hence, with decreasing the fraction of surface undercoordinated atoms), approaching the features observed in the spectrum of reference bulk SnO_2 .

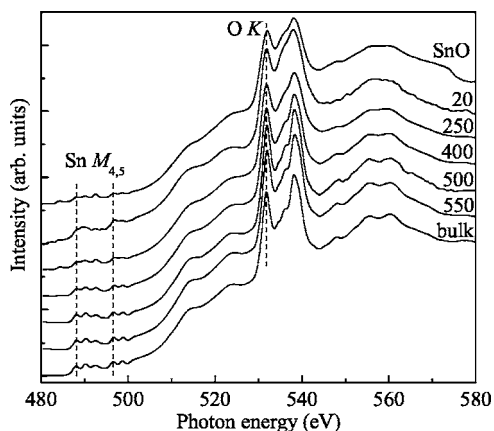


FIG. 2. Oxygen K -edge and Sn $M_{4,5}$ -edge XANES spectra of SnO_2 aerogels annealed at different temperatures as indicated (in $^\circ\text{C}$). Spectra taken from full-density rutile SnO_2 (labeled as “bulk”) and tetragonal SnO are also shown for comparison.

The low-intensity near-edge features of Sn $M_{4,5}$ spectra of aerogels are better illustrated in Fig. 3(a), which shows that, with an increase in the surface area, (i) an additional peak centered on ~ 4 eV appears and grows, (ii) the relative intensity of the peak at ~ 12 eV increases, and (iii) all the other peaks exhibit broadening. Such spectral broadening observed in Fig. 3(a) with an increase in the surface atom fraction is consistent with the behavior of O K -edge features in Fig. 2. Similar broadening has also been observed in several previous XANES studies of other semiconductor nanoparticles

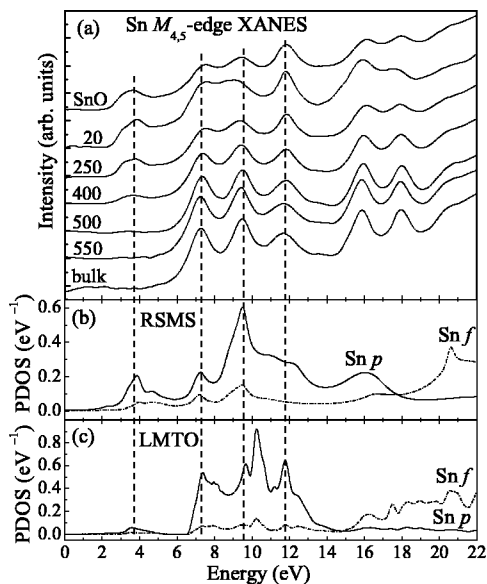


FIG. 3. (a) Tin $M_{4,5}$ -edge XANES spectra for SnO_2 aerogels annealed at different temperatures as indicated (in $^\circ\text{C}$). Spectra taken from full-density rutile SnO_2 (labeled as “bulk”) and tetragonal SnO are also shown for comparison. Angular momentum resolved PDOS of p and f character for Sn atoms in bulk rutile SnO_2 calculated by RSMS and LMTO methods are shown in (b) and (c), respectively. The features of $M_{4,5}$ -edge XANES spectra and PDOS were brought to the same energy scale with the conduction band minimum at zero energy.

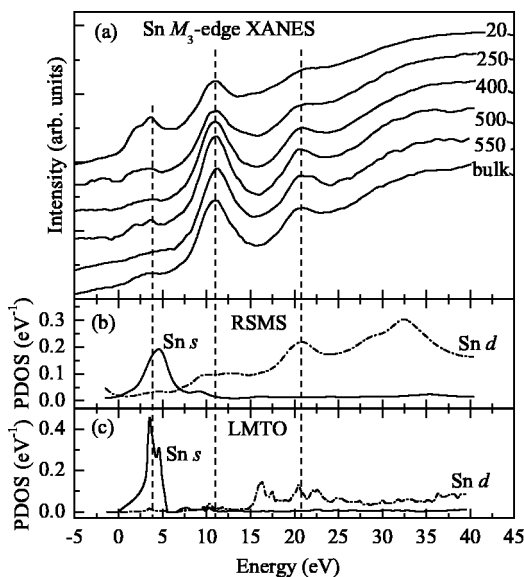


FIG. 4. (a) Tin M_3 -edge XANES spectra for SnO_2 aerogels annealed at different temperatures as indicated (in $^\circ\text{C}$). A spectrum taken from bulk rutile SnO_2 is also shown for comparison. Angular momentum resolved PDOS of s and d character for Sn atoms in bulk rutile SnO_2 calculated by RSMS and LMTO methods are shown in (b) and (c), respectively. The XANES spectra and PDOS were brought to the same energy scale with the conduction band minimum at zero energy. The strong peak centered on ~ 11 eV in the figure was at ~ 719 eV in the as-measured spectra.

(such as InAs, CdSe, and TiO_2) of similar sizes.³⁴ In addition, an increase in the intensity of the peak at ~ 12 eV in Fig. 3(a) can be attributed to an overlap of the main peak at this energy from the M_5 edge and the spin-orbit-split M_4 -edge counterpart of the additional surface-related feature which is at ~ 4 eV in M_5 -edge spectra.

To correlate the energy positions of peaks in Sn $M_{4,5}$ -edge spectra with conduction band features, Figs. 3(b) and 3(c) show Sn p - and f -projected PDOS calculated with RSMS and LMTO methods, respectively. In Fig. 3, the major peaks in $M_{4,5}$ -edge XANES spectra have been aligned with the corresponding features in theoretical PDOS curves, with the conduction band minimum (CBM) at zero energy. It is seen from Figs. 3(b) and 3(c) that relative peak intensities are different in PDOS predictions by these two (also significantly different) theoretical approaches. However, Fig. 3 shows that the energy positions of all three major features in spectra of bulk SnO_2 are well reproduced in the Sn PDOS of p and f character, particularly in the case of LMTO calculations. More importantly, such a comparison of theoretical PDOS and experimental XANES spectra shows that the additional (relatively intense) peak at ~ 4 eV, related to under-coordinated surface atoms, lies within the conduction band and not in the band gap.

An insight into the origin of such an additional surface-related peak comes from the fact that spectra of the as-prepared SnO_2 aerogel shown in Figs. 2 and 3(a) are similar to those of bulk tetragonal SnO. This finding is somewhat surprising since, as discussed above, our XRD and SAD analyses have revealed no evidence of the tetragonal SnO

phase in aerogels. These XANES results are, however, consistent with previous observations that valence-band XPS spectra of bulk SnO₂ often resemble those of SnO.¹⁶ Moreover, recent theoretical studies have predicted that energetically favorable reconstructions of SnO₂ (110) and (101) surfaces result in surface O deficiency.³⁵ Due to the large surface-to-volume atom fraction in aerogels, such O deficiency, related to the surface reconstruction, is revealed even with a technique (TEY XANES) that probes the entire volume of nanoligaments.

Finally, Fig. 4 shows a series of Sn *M*₃-edge XANES spectra of annealed aerogels [Fig. 4(a)] and corresponding Sn *s*- and *d*-projected PDOS calculated for bulk SnO₂ with RSMS [Fig. 4(b)] and LMTO [Fig. 4(c)] methods.³⁶ A relatively good correlation between the major features in experimental spectra and PDOS of *d* character is revealed in Fig. 4. By analogy with the above discussion of Sn *M*_{4,5} spectra (Fig. 3), Fig. 4 further supports the presence of an intense feature (centered on ~4 eV) related to additional Sn-related surface states. Figure 4 also shows that such additional Sn-related states (apparently, of *s* character) tail to the CBM, hence, playing an important role in the conductivity and gas sensing mechanisms of potential devices based on SnO₂

nanostructures. However, further work is currently needed for an atomic-level understanding of the surface reconstruction (as well as possible surface disorder and quantum confinement effects) responsible for the Sn-related surface states in SnO₂ aerogels revealed in the present study.

In conclusion, we have studied the unoccupied electronic states in nanocrystalline rutile SnO₂ aerogels with different fractions of undercoordinated surface atoms. A comparison of experimental spectra with theoretical densities of states has revealed additional Sn-related electronic states close to the conduction band minimum of aerogels as compared to the case of full-density SnO₂. These additional states are due to a large fraction of undercoordinated surface atoms and related to O-deficiency and a surface reconstruction of SnO₂ nanoparticles forming the aerogel solid network.

This work was performed under the auspices of the U.S. DOE by the University of California, LLNL under Contract No. W-7405-Eng-48. The ALS is supported by the Director, Office of Science, OBES, Materials Sciences Division, of the U.S. DOE under Contract No. DE-AC03-76SF00098. SSRL is a national user facility operated by Stanford University on behalf of the U.S. DOE, OBES.

*Corresponding author. Email address: kucheyev@llnl.gov

¹H. L. Hartnagel, A. L. Dewar, A. K. Jain, and C. Jagadish, *Semiconducting Transparent Thin Films* (IOP Publishing, Bristol, 1995).

²See, for example, N. Barsan, M. Schweizer-Berberich, and W. Gopel, *Fresenius' J. Anal. Chem.* **365**, 287 (1999).

³Y. Idota, T. Kubota, A. Matsufuji, Y. Maekawa, and T. Miyasaka, *Science* **276**, 1395 (1997).

⁴S. B. Ogale, R. J. Choudhary, J. P. Buban, S. E. Lofland, S. R. Shinde, S. N. Kale, V. N. Kulkarni, J. Higgins, C. Lanci, J. R. Simpson, N. D. Browning, S. Das Sarma, H. D. Drew, R. L. Greene, and T. Venkatesan, *Phys. Rev. Lett.* **91**, 077205 (2003).

⁵J. M. D. Coey, A. P. Douvalis, C. B. Fitzgerald, and M. Venkatesan, *Appl. Phys. Lett.* **84**, 1332 (2004).

⁶C. B. Fitzgerald, M. Venkatesan, A. P. Douvalis, S. Huber, J. M. D. Coey, and T. Bakas, *J. Appl. Phys.* **95**, 7390 (2004).

⁷Z. W. Pan, Z. R. Dai, and Z. L. Wang, *Science* **291**, 1947 (2001).

⁸E. Comini, G. Faglia, G. Sberveglieri, Z. W. Pan, and Z. L. Wang, *Appl. Phys. Lett.* **81**, 1869 (2002).

⁹M. Law, D. J. Sirbully, J. C. Johnson, J. Goldberger, R. J. Saykally, and P. D. Yang, *Science* **305**, 1269 (2004).

¹⁰J. Robertson, *J. Phys. C* **12**, 4767 (1979).

¹¹S. Munnix and M. Schmeits, *Phys. Rev. B* **27**, 7624 (1983); **33**, 4136 (1986).

¹²A. Svane and A. Antoncik, *J. Phys. Chem. Solids* **48**, 171 (1987).

¹³C. L. Lau and G. K. Wertheim, *J. Vac. Sci. Technol.* **15**, 622 (1978).

¹⁴D. F. Cox, T. B. Fryberger, and S. Semancik, *Phys. Rev. B* **38**, 2072 (1988).

¹⁵J. M. Themlin, R. Sporcken, J. Darville, R. Caudano, J. M. Gilles, and R. L. Johnson, *Phys. Rev. B* **42**, 11914 (1990); J. M. Themlin, M. Chtaiab, L. Henrard, P. Lambin, J. Darville, and J. M.

Gilles, *ibid.* **46**, 2460 (1992).

¹⁶R. Sanjines, C. Coluzza, D. Rosenfeld, F. Gozzo, Ph. Almeras, F. Levy, and G. Margaritondo, *J. Appl. Phys.* **73**, 3997 (1993).

¹⁷N. I. Medvedeva, V. P. Zhukov, M. Ya. Khodos, and V. A. Gubanov, *Phys. Status Solidi B* **160**, 517 (1990).

¹⁸K. C. Mishra, K. H. Johnson, and P. C. Schmidt, *Phys. Rev. B* **51**, 13972 (1995).

¹⁹Ph. Barbarat, S. F. Matar, and G. Le Blevennec, *J. Mater. Chem.* **7**, 2547 (1997).

²⁰C. Kilic and A. Zunger, *Phys. Rev. Lett.* **88**, 095501 (2002).

²¹J. Chouvin, J. Olivier-Fourcade, J. C. Jumas, B. Simon, P. H. Biensan, F. J. F. Madrigal, J. L. Tirado, and C. P. Vicente, *J. Electroanal. Chem.* **494**, 136 (2000).

²²C. McGuinness, C. B. Stagaescu, P. J. Ryan, J. E. Downes, D. F. Fu, K. E. Smith, and R. G. Egdell, *Phys. Rev. B* **68**, 165104 (2003).

²³M. S. Moreno, R. F. Egerton, and P. A. Midgley, *Phys. Rev. B* **69**, 233304 (2004); M. S. Moreno, R. F. Egerton, J. J. Rehr, and P. A. Midgley, *ibid.* **71**, 035103 (2005).

²⁴A. L. Ankudinov, B. Ravel, J. J. Rehr, and S. D. Conradson, *Phys. Rev. B* **58**, 7565 (1998).

²⁵A. Cabot, J. Arbiol, R. Ferre, J. R. Morante, F. Chen, and M. Liu, *Appl. Phys. Lett.* **95**, 2178 (2004).

²⁶See, for example, a review by T. F. Baumann, A. E. Gash, G. A. Fox, J. H. Satcher, Jr., and L. W. Hrubesh, in *Handbook of Porous Solids*, edited by F. Schuth, K. S. W. Sing, and J. Weitkamp (Wiley-VCH, Weinheim, 2002).

²⁷T. F. Baumann, S. O. Kucheyev, A. E. Gash, and J. H. Satcher, Jr., *Adv. Mater.* **17**, 1546 (2005).

²⁸L. W. Hrubesh, T. M. Tillotson, and J. F. Poco, in *Chemical Processing of Advanced Materials*, edited by L. L. Hench and J. K. West (Wiley, New York, 1992), p. 19.

- ²⁹O. K. Andersen, Phys. Rev. B **12**, 3060 (1975).
- ³⁰Note that FEFF calculations with the core holes included revealed relatively minor changes in the PDOS of SnO₂ (such as some changes in relative peak intensities and expected energy shifts) as compared to the ground state PDOS reported in this article.
- ³¹An increase in the effective surface area and pore volume after annealing at 250 °C (see Table I) can be attributed to the desorption of residual organic species from the aerogel surface.
- ³²See, for example, J. Stöhr, *NEXAFS Spectroscopy* (Springer, Berlin, 1996).
- ³³The spin-orbit-split broad, intense features at ~515 and 523 eV in Fig. 2 are due to $3d \rightarrow \epsilon f$ transitions. A discussion of such transitions, related to a non-coulombic nature of the potential, can be found in a review by J. P. Connerade, Contemp. Phys. **19**, 415 (1978).
- ³⁴K. S. Hamad, R. Roth, J. Rockenberger, T. van Buuren, and A. P. Alivisatos, Phys. Rev. Lett. **83**, 3474 (1999); L. Soriano, P. P. Ahonen, E. I. Kauppinen, J. Gomez-Garcia, C. Morant, F. J. Palomares, M. Sanchez-Agudo, P. R. Bressler, and J. M. Sanz, Monatsch. Chem. **133**, 849 (2002).
- ³⁵M. A. Mäki-Jaskari and T. T. Rantala, Phys. Rev. B **65**, 245428 (2002); M. Batzill, A. M. Chaka, and U. Diebold, Europhys. Lett. **65**, 61 (2004); W. Bergermayer and I. Tanaka, Appl. Phys. Lett. **84**, 909 (2004).
- ³⁶Compared to the case of Sn $M_{4,5}$ -edge spectra (Figs. 2 and 3), in such Sn M_3 -edge spectra in Fig. 4, all features are broadened due to a short lifetime of $3p$ core holes.